

# Enhanced Magnetization by Defect-Assisted Exciton Recombination in Atomically Thin CrCl<sub>3</sub>

Xin-Yue Zhang,<sup>1</sup> Thomas K. M. Graham,<sup>1</sup> Yu-Xuan Wang,<sup>1</sup> Hyeonhu Bae,<sup>2</sup> Nazar Deegan,<sup>3,4</sup> Zhi-Cheng Wang,<sup>1</sup> Jakub Regner,<sup>5</sup> Kenji Watanabe,<sup>6</sup> Takashi Taniguchi,<sup>7</sup> Minkyung Jung,<sup>8</sup> Zdeněk Sofer,<sup>5</sup> Fazel Tafti,<sup>1</sup> David D. Awschalom,<sup>3,4</sup> F. Joseph Heremans,<sup>3,4</sup> Binghai Yan,<sup>2</sup> and Brian B. Zhou<sup>1,\*</sup>

<sup>1</sup>*Department of Physics, Boston College, Chestnut Hill, MA, 02467, USA*

<sup>2</sup>*Department of Condensed Matter Physics, Weizmann Institute of Science, Rehovot, Israel*

<sup>3</sup>*Center for Molecular Engineering, Materials Science Division, Argonne National Laboratory, Lemont, IL, 60439, USA*

<sup>4</sup>*Pritzker School of Molecular Engineering, University of Chicago, Chicago, IL 60637, USA*

<sup>5</sup>*Department of Inorganic Chemistry, University of Chemistry and Technology Prague, Technická 5, 166 28, Prague 6, Czech Republic*

<sup>6</sup>*Research Center for Electronic and Optical Materials, National Institute for Materials Science, 1-1 Namiki, Tsukuba 305-0044, Japan*

<sup>7</sup>*Research Center for Materials Nanoarchitectonics, National Institute for Materials Science, 1-1 Namiki, Tsukuba 305-0044, Japan*

<sup>8</sup>*DGIST Research Institute, DGIST, Daegu 42988, Republic of Korea*

(Dated: December 15, 2023)

Two dimensional (2D) semiconductors present unique opportunities to intertwine optical and magnetic functionalities and to tune these performances through defects and dopants. In 2D semiconductors, the properties of excitons often vary due to the underlying magnetic order, but the modification of their magnetic properties by excitonic processes remains difficult to achieve. Here, we integrate exciton pumping into a quantum sensing protocol on nitrogen-vacancy centers in diamond to image the optically-induced transient stray fields in few-layer, antiferromagnetic CrCl<sub>3</sub>. We discover that exciton recombination enhances the in-plane magnetization of the CrCl<sub>3</sub> layers, with an outsized effect in the surface monolayers and when the surface is unencapsulated. Concomitantly, time-resolved photoluminescence measurements reveal that a defect-assisted Auger recombination dominates for atomically thin CrCl<sub>3</sub> with tightly localized, nearly forbidden excitons and amplified surface-to-volume ratio. These experimental signatures establish the magnetically enhanced state to result from an exciton-activated electron transfer between surface impurities and the spin-polarized conduction band. Density functional theory calculations identify that the mediating impurity state could originate from oxygen adsorbates with spins antiparallel to the magnetization of their host layer. Our work unambiguously demonstrates the tunability of single intrinsic magnetic layers via defect engineering and opens a pathway to dynamically reconfigure these effects in devices through optical control.

Magnetic order in 2D semiconductors can modulate their reflection [1, 2] or absorption [3] of polarized light, as well as the polarization [4, 5] or spectrum [6] of their photoluminescence (PL). These magneto-optical effects, which allow sensitive optical probing of the underlying magnetization, often hinge on the special properties of bound electron-hole pairs, known as excitons, that exhibit the enhanced Coulomb interactions [7, 8], spin-valley coupling [9], or interlayer hybridization [6] of the 2D limit. An intriguing prospect is whether the inverse effect occurs: can excitonic processes in a 2D semiconductor modify its magnetic properties? Such optical control of magnetism could enable low-power, high-speed spintronic devices featuring the versatility of the 2D materials platform [10–12].

Recent theoretical works have highlighted the role of strongly bound excitons in the giant magneto-optical response of the atomically thin chromium trihalides (CrX<sub>3</sub>,

X = Cl, Br, I) [7, 8]. Strikingly in CrX<sub>3</sub>, the exciton binding energy exceeds several volts [13–15], as compared to several hundred millivolts, already a large value, in the monolayer transition metal dichalcogenides (TMDs) [16]. Due to weaker *dp* hybridization between the Cr ion and lighter halogen atoms, CrCl<sub>3</sub> possesses the tightest exciton localization among the CrX<sub>3</sub>, with its exciton wave function nearly confined to a single CrX<sub>3</sub> octahedron [14, 15]. These localized excitons derive from the nominally parity-forbidden *d-d* transitions of atomic Cr in a crystal field, possessing characteristics akin to Frenkel excitons in molecular systems. Accordingly, their recombination dynamics and interactions with the environment can differ sharply from delocalized Wannier-Mott excitons. In bulk and molecular systems, excitonic processes are known to modulate magnetism through, for example, driving charge transfer [17, 18] and altering exchange interactions [19, 20]. However, their effects in atomically thin magnets, particularly those mechanisms that stand out in the 2D limit, have yet to be fully elucidated.

In this work, we introduce pump-probe nitrogen-vacancy (NV) center magnetometry for the spinotem-

---

\* [brian.zhou@bc.edu](mailto:brian.zhou@bc.edu)

poral imaging of optically controlled magnetism. By pumping the excitonic resonances in few-layer, antiferromagnetic (AF)  $\text{CrCl}_3$ , we discover that its in-plane, layer-alternating magnetization is remarkably increased within the pump spot by up to  $0.5 \mu_B/\text{nm}^2$  in odd-layer regions, where  $\mu_B$  is the Bohr magneton. The transient stray field due to this optical enhancement provides sensitive even-odd layer contrast as a local signature in the flake's interior, in distinction to the static stray field that diminishes away from the edges.

We link the formation of the magnetically enhanced state to a defect-assisted Auger recombination [21, 22] that predominates for excitons in  $\text{CrCl}_3$  with singularly long radiative lifetimes and strong electron-hole overlap [15]. Time-resolved PL measurements probing the dynamics of exciton recombination reveal that this nonradiative pathway intensifies in thinner flakes and hence is mediated by surface defects. In concert, transient magnetization measurements on a spin-flipped even layer and on contiguous regions encapsulated and unencapsulated by hexagonal boron nitride (hBN) demonstrate that the optical enhancement is primarily contributed by the surface monolayers and is sensitive to surface condition.

Our density functional theory (DFT) calculations explain that Auger recombination can enhance the magnetization of  $\text{CrCl}_3$  by transferring minority spin defect electrons from oxygen adsorbates into the majority spin conduction band of their host layer. Our results therefore provide a conclusive demonstration of defect-modulation of the magnetic properties of single atomic layers with intrinsic order. Although proposed in computational studies [23–25], this tuning knob, with strategies unique to the 2D limit such as molecular adsorption [26–28], has eluded experimental realization due to stringent requirements on control samples and quantitative magnetic measurement. Fundamentally, the exciton-activated charge transfer alters the occupation of the  $t_{2g}$  and  $e_g$  Cr orbitals and accordingly, the underlying exchange pathways. It can drive not only an increase in magnetic moment as detected here, but also an increase in Néel or Curie temperature [23, 26, 27], or change in magnetic ground state [24] or anisotropy [28]. Hence, our discovery achieves a compelling step towards the multifaceted optical control of atomically-thin magnets, with advantages in spatial resolution, bandwidth, and efficiency.

### A. In-Plane, AF Interlayer Order

Below its Néel temperature  $T_N \approx 17$  K, bulk  $\text{CrCl}_3$  possesses moments that order ferromagnetically in-plane within each layer, but antiferromagnetically between adjacent layers [29]. As in-plane magnetization cannot be detected via magneto-optical effects using light at normal incidence, magnetic order in atomically-thin  $\text{CrCl}_3$  has only been investigated by tunneling magnetoresistance [30–33] and x-ray magnetic circular dichroism at grazing incidence [34], which both possess limited spatial

resolution. To overcome this lack of spatial information, we leverage magnetic imaging by NV spins in diamond, previously employed to visualize the out-of-plane magnetic order in  $\text{CrI}_3$  and  $\text{CrBr}_3$  [35–37]. In extension to prior works, here we implement a geometry optimized for high-sensitivity ac magnetometry [38] and pump-probe optical access [39]. Few-layer  $\text{CrCl}_3$  flakes, encapsulated by hBN unless otherwise described, are transferred inside an argon-filled glovebox onto a  $^{12}\text{C}$  isotopically-enriched diamond substrate containing a near-surface NV ensemble with prolonged coherence time (Appendix A). As illustrated in Figs. 1a,b, the pump beam of variable wavelength (405–785 nm; shown in red) excites exciton dynamics in  $\text{CrCl}_3$ , while an independently steered probe beam (green, 515 nm) images the resulting stray magnetic field across the NV ensemble at diffraction-limited spatial resolution.

We begin by performing pulsed optically detected magnetic resonance (ODMR) to determine the static, layer-dependent magnetization in  $\text{CrCl}_3$  flakes at  $T = 4$  K. In this mode, the NV spin transitions are Zeeman-shifted by the dc stray field along the NV center axis, angled at  $\theta = 35^\circ$  from the surface in the  $xz$ -plane (Fig. 1a) [35]. We apply a bias field  $B_{ext}$  along the NV center axis and define the quantity  $B_{NV}$  to be solely the field due to the flake by subtracting  $B_{ext}$  from the measured total field.

Figure 1c shows the image of  $B_{NV}$  at small  $B_{ext} = 3.3$  mT for the  $\text{CrCl}_3$  flake depicted in Fig. 1a, containing regions with four to nine layers. Significant stray fields are detected over the odd-layer regions, in contrast to negligible stray fields over the even-layer regions, except over a narrow 6/8-layer stripe where the signal is contributed by its two neighboring odd layers. In Fig. 1d, we simulate the flake's stray field assuming AF interlayer magnetic order oriented along the in-plane projection of  $B_{ext}$  ( $+\hat{x}$ ) [40]. This simulation reproduces the salient even-odd stray field contrast, as well as the detailed spatial parity of the stray field, which is inconsistent with out-of-plane magnetic order (Supplementary Fig. 1). Quantitative linecuts presented in Supplementary Fig. 1e reveal that the areal magnetization of the 5/7-layer stripe is approximately  $14 \mu_b/\text{nm}^2$ , slightly reduced from the expected saturation magnetization of a single uncompensated layer ( $19 \mu_b/\text{nm}^2$ ).

Importantly for later discussions, we observe a reversal of the direction of the stray field over the narrow 6/8-layer stripe when  $B_{ext}$  is increased to 141.5 mT (Fig. 1e). Our simulation (Fig. 1f) and extracted linecut (Supplementary Fig. 1i) explain that this reversal corresponds to the flipping of a single layer that is anti-aligned with the external field, such that the net magnetization of the even-layer stripe increases from approximately fully-compensated to two uncompensated layers ( $28 \mu_B/\text{nm}^2$ ). For the outer even-layer regions (4 and 6-layer), the stray fields at their boundaries become stronger at  $B_{ext} = 141.5$  mT, with a weak positive field in the 6-layer's interior, signaling the emergence of finite magnetizations due to canting of the spins out of the plane.

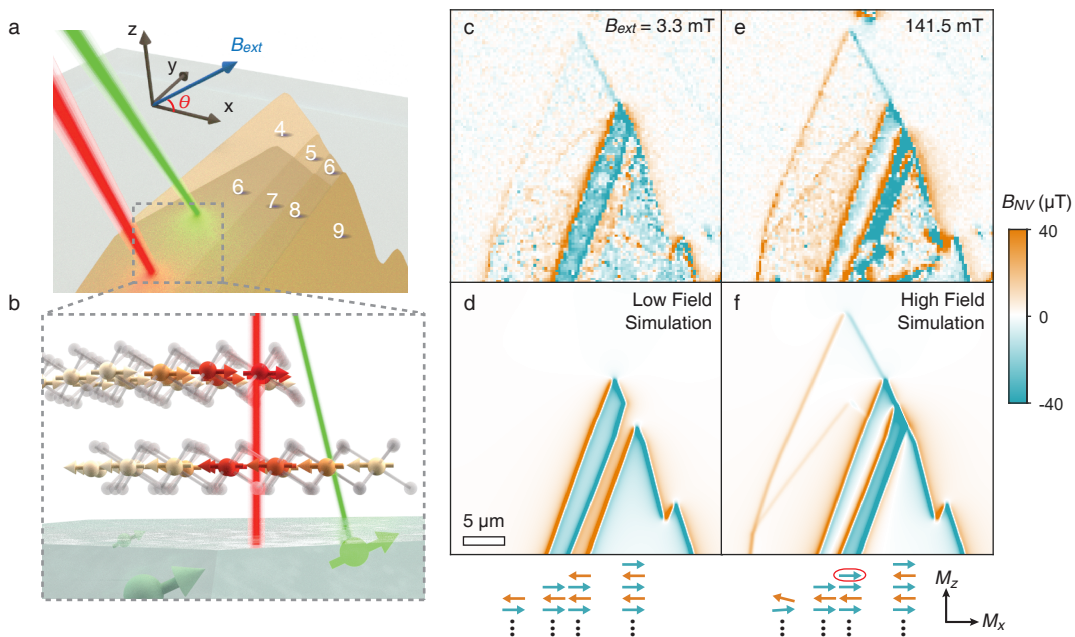


FIG. 1. Experimental background. (a) Few-layer  $\text{CrCl}_3$  flakes are transferred onto a diamond substrate (gray) containing a near-surface ensemble of NV centers. NV magnetic imaging is performed by scanning the green probe beam (515 nm), while exciton dynamics in  $\text{CrCl}_3$  are stimulated by the “red” pump beam (variable wavelength). (b) The layer magnetization in  $\text{CrCl}_3$  lies in-plane and alternates antiferromagnetically between layers, producing a stray magnetic field sensed by proximal NV centers (green). (c) Experimental dc stray field ( $B_{NV}$ ) image of a  $\text{CrCl}_3$  flake, with 4 to 9-layer regions as labeled in panel a), at low external field  $B_{ext}$ . (d) Simulation of  $B_{NV}$  assuming in-plane, AF interlayer order. The bottom cartoon displays the magnetization of the top-most layers for the vertically adjacent region, showing odd-layer regions to possess an uncompensated monolayer along the in-plane projection of  $B_{ext}$ . (e) Experimental  $B_{NV}$  image at high  $B_{ext}$ . (f) Simulation of  $B_{NV}$  assuming that one layer of spins (circled) within the 6/8-layer stripe flips, resulting in two uncompensated layers.

## B. Optical Modulation of Néel Magnetization

Having established the underlying in-plane, layered AF state, we now uncover a startling optical effect on the Néel magnetization of atomically thin  $\text{CrCl}_3$ . Figure 2a displays the dc stray field image at  $B_{ext} = 141.5$  mT for another  $\text{CrCl}_3$  flake containing 5, 6, and 8-layer regions. Significant  $B_{NV}$  is again only observed over the odd-layer area.

Using only the green NV probe beam, we switch to a Hahn echo sequence for sensing dynamic fields. Here, the NV center is prepared in a superposition state and allowed to precess over a free evolution time  $2\tau$ , separated into two halves by a  $\pi$ -pulse (Fig. 2b). The total precession angle  $\Phi$  is determined from  $\Phi = \arctan(Y_P/X_P)$ , where  $X_P$  and  $Y_P$  are the X- and Y-axis Bloch sphere projections of the final state (Appendix B). If the stray magnetic field is static over the  $2\tau$  evolution, the precession during the first half exactly cancels that over the second half, and  $\Phi = 0$ . This trivial behavior is indeed observed over the bare NV substrate (0-layer), such that  $Y_P$  remains fixed at 0 and  $X_P$  decays smoothly due to quantum decoherence as the evolution time is lengthened (Fig. 2c). Unexpectedly, when we perform the Hahn echo over the 5-layer region,  $Y_P$  displays a pronounced

increase before being bounded by the decoherence envelope, revealing that the precession angle  $\Phi$  increases with evolution time (Fig. 2d). The same experiment on the 6-layer region, however, exhibits only faster decoherence compared to the bare substrate due to magnetic fluctuations in  $\text{CrCl}_3$ , but negligible coherent phase accumulation (Fig. 2e).

By scanning the green beam over the diamond and  $\text{CrCl}_3$ , we spatially image the accumulated  $\Phi$  for a Hahn echo sequence with fixed evolution time  $2\tau = 13 \mu\text{s}$  (Fig. 2f). We observe nearly homogeneous phase precession over the 5-layer region, but negligible precession over the 6 and 8-layer regions. For particular conditions, this imaging scheme can be significantly faster than ODMR for distinguishing even and odd layers due to its strong signal in the flake’s interior, independent of the flake’s dimensions, and fewer data points needed per pixel (Appendix B).

Our results clearly indicate that a time-varying magnetization  $\Delta M(t)$  is stimulated in the  $\text{CrCl}_3$  flake (e.g., a decaying exponential as diagrammed in Fig. 2b), such that its stray field is not constant over the two halves of the Hahn echo. One reasonable, but inconsistent, hypothesis is that NV center probe laser locally heats the  $\text{CrCl}_3$  flake, causing a transient demagnetization that gradually recovers during the intervening laser off pe-

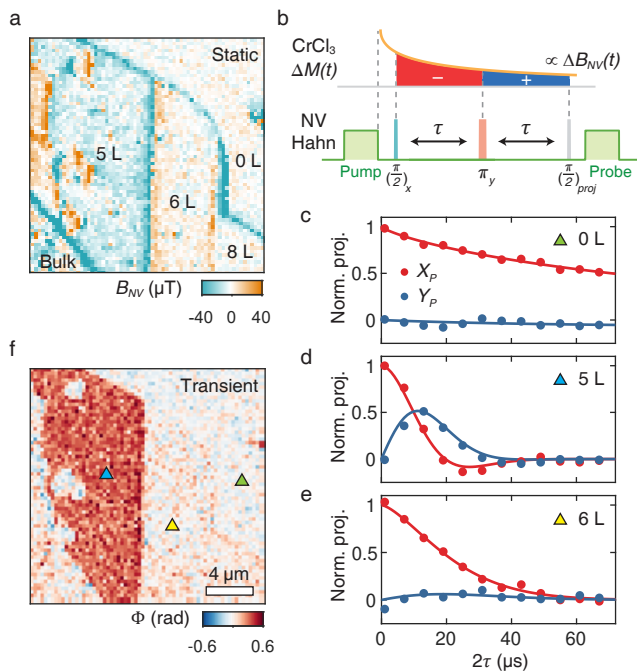


FIG. 2. Transient stray fields from optically-excited  $\text{CrCl}_3$ . (a) Preliminary: dc stray field ( $B_{NV}$ ) image identifying 5, 6, 8-layer and bulk regions of a  $\text{CrCl}_3$  flake. (b) Schematic of a Hahn echo sequence with total duration  $2\tau$  applied to the NV center, alongside a temporally decaying magnetic field  $\Delta B_{NV}(t)$  due to a magnetization change  $\Delta M(t)$  in  $\text{CrCl}_3$  induced by the initial green pulse (power  $P = 80 \mu\text{W}$ ). The  $\pi$ -pulse negates the phase accumulated during the first half of the evolution. (c,d,e) Hahn echo measured over: c) the bare NV substrate (0-layer), d) 5-layer region, and e) 6-layer region. Only the 5-layer region engenders a non-zero NV precession angle  $\Phi$ , indicated by the simultaneous evolution of the  $X_P$  and  $Y_P$  projections of the NV superposition state with increasing Hahn echo duration. (f) Image of the precession angle  $\Phi$ , reflecting the optically-induced transient stray field, for an Hahn echo sequence with  $2\tau = 13 \mu\text{s}$  over the same region as a) by scanning the single green beam ( $B_{ext} = 141.5 \text{ mT}$ ).

riod. If thermal demagnetization were the mechanism, we would expect  $\Phi$  to saturate when  $2\tau$  significantly exceeds the thermal time constant ( $\approx 1 \mu\text{s}$ ) (Supplementary Section IV) [42]. However, the experimental  $\Phi$  is growing over tens of microseconds (Fig. 2d), indicating a much longer magnetization recovery time. Moreover, we will show that the spatial distribution of the transient stray field corresponds to an *enhancement*, rather than a reduction, of the in-plane magnetization.

### C. Pump-Probe Imaging of Locally Enhanced Magnetization

By incorporating a second laser dedicated to pumping  $\text{CrCl}_3$ , we can scan the NV probe beam while holding the  $\text{CrCl}_3$  excitation fixed to map the stray field profile of

the optically-induced magnetization. We pulse the pump laser after the NV probe laser has been turned off for at least  $50 \mu\text{s}$  to allow the incidental effect of the probe to decay (Fig. 3a). Crucially, the Hahn echo is still required for sensitivity, as dc sensing with the pump laser on cannot resolve the small magnetization difference.

Figure 3b shows images of the transient stray field as a function of temperature upon exciting the 7-layer stripe of Fig. 1a with a pump wavelength  $\lambda = 730 \text{ nm}$ . The spatially-resolved  $\Phi(\mathbf{r})$ , where  $\mathbf{r}$  is the position of the probe beam relative to the pump, displays a double-lobe, sign-switching feature, which remains virtually unchanged up to a few Kelvin below  $T_N$ , but disappears at  $18 \text{ K}$  (above  $T_N$ ). Notably, the positive lobe (red) in  $\Phi(\mathbf{r})$  includes the center point where the pump and probe beams coincide (yellow circle), consistent with the sign for  $\Phi$  measured when the single NV beam serves as both pump and probe (Fig. 2f). Supplementary Fig. 2 displays the typical dependence of the maximal  $\Phi$  on the pump fluence, showing it to saturate for high powers  $P$  or long pulse widths  $t_p$ .

At  $B_{ext} = 141.5 \text{ mT}$ , the phase accumulated by our sensing state during the Hahn echo is given by an integral of the transient stray field  $\Delta B_{NV}(t)$ :

$$\Phi(2\tau, t_d) = 2\pi\gamma_e \left( \int_{t_d+\tau}^{t_d+2\tau} \Delta B_{NV}(t') dt' - \int_{t_d}^{t_d+\tau} \Delta B_{NV}(t') dt' \right). \quad (1)$$

Measurements using a simulated waveform for  $\Delta B_{NV}(t)$  corroborate that positive  $\Phi$  corresponds to  $\Delta B_{NV}$  that is more negative (antiparallel to the NV axis) in the first half of the Hahn echo sequence than in the second half (Supplementary Section IV).

The localized pattern for  $\Phi(\mathbf{r})$  (Fig. 3b) motivates us to consider a Gaussian profile, following the pump beam intensity, for the optically-induced magnetization  $\Delta M(\mathbf{r}, t)$ . In Fig. 3c, we simulate the additional stray field  $\Delta B_{NV}(\mathbf{r})$  produced by  $\Delta M(\mathbf{r})$  corresponding to an enhancement of the in-plane magnetization along the  $+\hat{x}$  direction with Gaussian amplitude and full-width-half-maximum of  $1.0 \mu\text{m}$  (black circle), approximately the pump beam size. The time-integrated  $\Phi(\mathbf{r})$  measured by Hahn echo should then display the same spatial distribution as  $-\Delta B_{NV}(\mathbf{r})$  since  $\Delta B_{NV}(\mathbf{r}, t)$  decays towards zero during the echo duration (Eq. 1).

The excellent correspondence between the experimental (Fig. 3b) and simulated patterns (Fig. 3c) demonstrates that below  $T_N$ , the existing in-plane magnetization is locally enhanced by optical excitation. Alternatively, we can allow the Gaussian enhancement  $\Delta M(\mathbf{r})$  to be oriented along an arbitrary angle  $\theta_m$  in the  $xz$ -plane (Supplementary Fig. 3). In this analysis,  $\theta_m \approx 0^\circ$  ( $+\hat{x}$ ) still produces the best fit to the experimental  $\Phi(\mathbf{r})$  image. To explain the even-odd contrast in the observable  $\Delta B_{NV}$  (Fig. 2f), we plausibly suppose that the enhancement  $\Delta M$  in each  $\text{CrCl}_3$  layer, if any, occurs along the magnetization direction of that layer. Then  $\Delta B_{NV}$

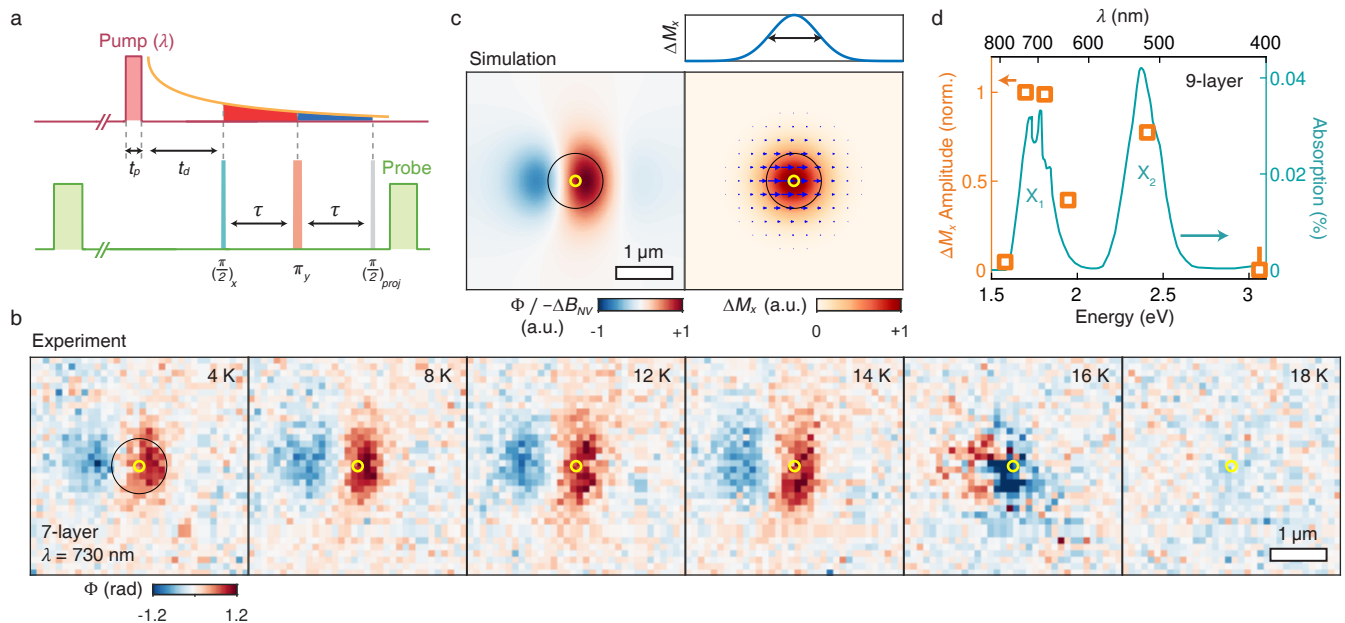


FIG. 3. Pump-probe imaging of exciton-enhanced magnetization. (a) Experimental timeline integrating a pump beam (wavelength  $\lambda$ ) into the Hahn echo sequence. The pump pulse of width  $t_p$  occurs at least  $50 \mu\text{s}$  after the initial green pulse (NV initialization); the Hahn echo is commenced after a delay  $t_d$  from the pump pulse. (b) Temperature evolution of the local Hahn precession angle  $\Phi(\mathbf{r})$  on a 7-layer region, measured by scanning the probe beam relative to a fixed pump beam at the yellow circle.  $\Phi(\mathbf{r})$  images the spatial distribution of the transient stray field induced by the pump beam ( $\lambda = 730 \text{ nm}$ ,  $P = 220 \mu\text{W}$ ,  $t_p = 1.2 \mu\text{s}$ ,  $t_d = 0$ ,  $2\tau = 13 \mu\text{s}$ ). (c) Left: simulation of the additional stray magnetic field  $\Delta B_{NV}(\mathbf{r}) \propto -\Phi(\mathbf{r})$  due to a Gaussian enhancement of the in-plane magnetization  $\Delta M_x(\mathbf{r})$ . Right: Spatial distribution and linecut of the simulated  $\Delta M_x(\mathbf{r})$  with the black circle and double arrow denoting the full width at half maximums. (d) Dependence of the magnetization enhancement amplitude (normalized by  $\lambda = 730 \text{ nm}$ ) on the pump wavelength  $\lambda$  for a 9-layer region. The overlaid teal curve denotes the expected optical absorption for a 9-layer flake, revealing two exciton peaks  $X_1$  and  $X_2$  (absorption data derived from Ref. [41]).

would be canceled over even layer areas due to AF interlayer coupling, although the underlying effect occurs everywhere.

As  $T_N$  is approached upon warming to 16 K, the  $\Phi(\mathbf{r})$  pattern nearly inverts for this specific flake (Fig. 3b). A higher resolution temperature sweep for a different 7-layer flake, presented in Supplementary Fig. 4, shows a rapid series of changes in  $\Phi(\mathbf{r})$ , including progressive rotations of its symmetry axis, near  $T_N$ . In first-principles calculations, an increase in magnetization is frequently associated with an enhanced transition temperature [23, 24, 26, 27]. In one scenario, the former results from a change in the valence of some of the Cr ions, thus opening a double-exchange pathway that strengthens ferromagnetic intralayer coupling [23, 24]. Deducing such effects from the subtle patterns in  $\Phi(\mathbf{r})$  upon crossing  $T_N$  is of future interest, but requires disentangling enhanced domain or laser heating effects near criticality [43].

#### D. Role of strongly bound Excitons

We focus our attention to understanding the robust magnetization enhancement below  $T_N$  by studying its

dependence on the  $\text{CrCl}_3$  excitation wavelength. Supplementary Fig. 5 shows  $\Phi(\mathbf{r})$  imaged on a 9-layer flake at six different pump wavelengths  $\lambda$  between 405 nm and 785 nm. We fit  $\Phi(\mathbf{r})$  for each  $\lambda$  according to the Gaussian model (Fig. 3c) with the beam width and amplitude  $\Delta M_x$  of the magnetization enhancement along the  $\hat{x}$ -direction as free parameters. Figure 3d shows the extracted  $\Delta M_x$  as a function of  $\lambda$ , normalized by the highest enhancement at  $\lambda = 730 \text{ nm}$ . In the same figure, we overlay the optical absorption spectrum of  $\text{CrCl}_3$  calculated from data at 4.2 K in Ref. [41], which displays a striking correlation to the optical enhancement.

The prominent absorption peaks at  $\sim 1.7 \text{ eV}$  and  $\sim 2.4 \text{ eV}$  correspond to the two lowest energy bright excitons ( $X_1$  and  $X_2$ ) identified in recent many-body perturbation theory calculations of  $\text{CrCl}_3$  excited states [14, 15]. The highest energy valence and lowest energy conduction bands in  $\text{CrCl}_3$  are primarily contributed, respectively, by the crystal-field split, majority spin  $t_{2g}$  and  $e_g$   $d$ -orbitals of Cr. Although  $d$ - $d$  transitions are strictly optically forbidden by Laporte rule, spin-orbit coupling and hybridization with the halogen  $p$ -orbitals, which both increase with halogen size, can render the transitions weakly-allowed [4, 15]. In  $\text{CrX}_3$ ,  $dp$ -hybridization also increases the bandwidth of the  $d$ -bands, where flat dis-

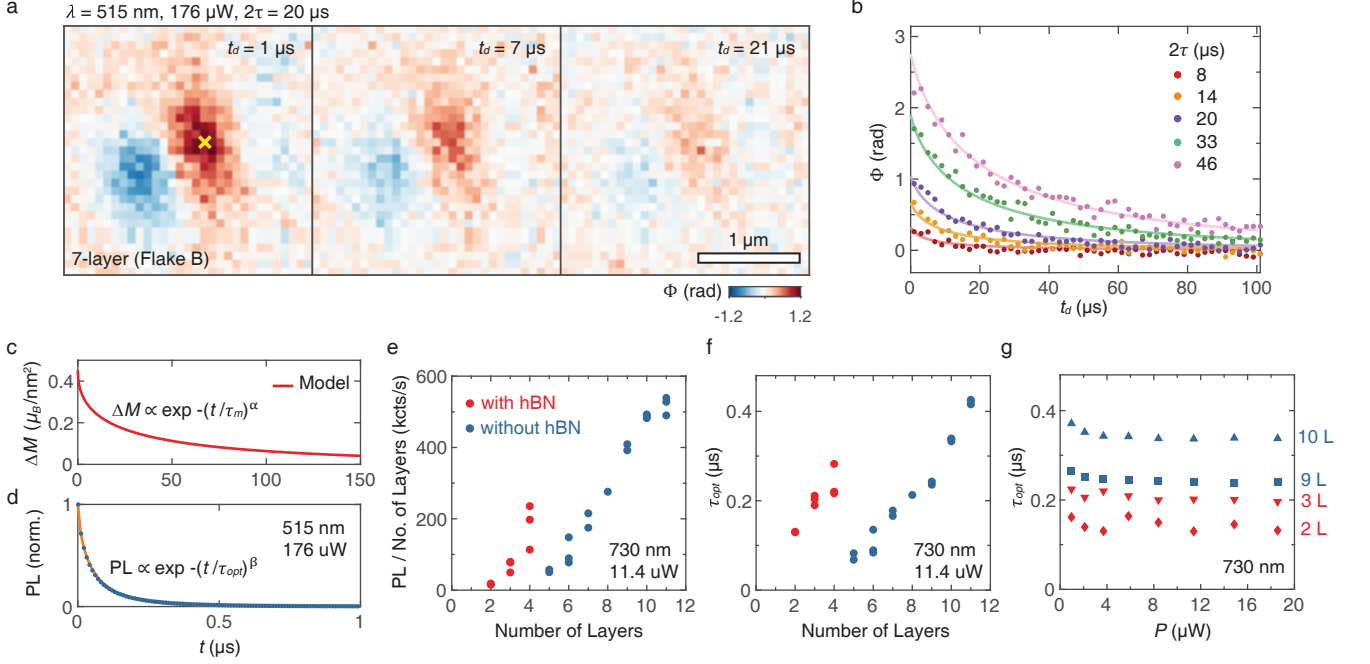


FIG. 4. Time-resolved magnetization and PL measurements. (a) Spatiotemporal images of  $\Phi(\mathbf{r})$  for various delays  $t_d$  between the pump pulse and Hahn echo sequence on 7-layer  $\text{CrCl}_3$ . The rotation of the  $\Phi(\mathbf{r})$  symmetry axis away from the  $+x$ -direction here is atypical for 4 K and likely reflects a local in-plane anisotropy that competes with the external field  $B_{ext}$ . (b) Hahn echo phase  $\Phi$  measured at the yellow cross in a) as a function of the pump-probe delay  $t_d$  and total echo duration  $2\tau$ . The solid lines are simultaneous best fit curves using a magnetization decay model  $\Delta M(t) = \Delta M_0 \exp(-(t/\tau_m)^\alpha)$ . (c) Inferred magnetization decay from b), yielding  $\Delta M_0 = 0.46 \mu_B/\text{nm}^2$ ,  $\tau_m = 26 \mu\text{s}$ , and  $\alpha = 0.5$ . (d) Decay of the PL intensity for 7-layer  $\text{CrCl}_3$  after excitation with  $\lambda = 515 \text{ nm}$  ( $X_2$ ). The solid best fit line extracts a long exciton lifetime  $\tau_{opt} = 38 \text{ ns}$  and exponent  $\beta = 0.6$ . (e) PL intensity per layer versus number of  $\text{CrCl}_3$  layers for  $\lambda = 730 \text{ nm}$  excitation ( $X_1$ ). (f) Exciton lifetime  $\tau_{opt}$  versus number of  $\text{CrCl}_3$  layers for  $\lambda = 730 \text{ nm}$ , with  $\beta = 0.79$  fixed for all. (g) Dependence of  $\tau_{opt}$  on the excitation power  $P$  for selected layer thicknesses. The red (blue) points in e), f), g) denote data from regions encapsulated (not encapsulated) by hBN.

persions enhance the localization and binding energy of their derived excitons. Hence, excitons in  $\text{CrCl}_3$  are expected to be the darkest and most tightly bound, while they are the brightest and most delocalized in  $\text{CrI}_3$ .

To clarify the role of the unique excitonic properties of  $\text{CrCl}_3$ , we compare the lifetime of the optically-induced magnetization  $\tau_m$  to the exciton lifetime  $\tau_{opt}$ . In Fig. 4a, we visualize the decay of  $\Phi(\mathbf{r})$  for increasing delay  $t_d$  between the pump pulse and Hahn echo sequence on a 7-layer region. To quantitatively extract  $\tau_m$ , we park the probe at the position of highest intensity in  $\Phi(\mathbf{r})$  (yellow cross in Fig. 4a) and measure the acquired  $\Phi$  as a function of both the delay  $t_d$  and total evolution time  $2\tau$  (Fig. 4b). We then use Eq. 1 to simultaneously fit this set of curves, assuming a phenomenological form of the magnetization decay  $\Delta M(t) = \Delta M_0 \exp(-(t/\tau_m)^\alpha)$  that creates  $\Delta B(t)$  through the Gaussian model (Supplementary Section V). The best-fit  $\Delta M(t)$  curve is plotted in Fig. 4c, displaying an estimated magnetization lifetime  $\tau_m = 26 \pm 3 \mu\text{s}$  with exponent  $\alpha = 0.5 \pm 0.1$  and a maximal magnetization change  $\Delta M_0 = 0.46 \pm 0.1 \mu_B/\text{nm}^2$ .

In contrast, the time-resolved PL intensity for  $\text{CrCl}_3$  (Fig. 4d), isolated with a 800 nm long-pass filter [30], completely decays within  $1 \mu\text{s}$ , indicating an exciton life-

time  $\tau_{opt} \approx 40 \text{ ns}$  for 515 nm excitation ( $X_2$ ). This  $\tau_{opt}$ , which would be even longer absent nonradiative relaxation, significantly exceeds both the bright ( $\sim 1 \text{ ps}$ ) and dark ( $\sim 100 \text{ ps}$ ) exciton lifetimes in monolayer TMDs [16], highlighting the extreme darkness of excitons in  $\text{CrCl}_3$ . However, since  $\tau_{opt}$  is yet two orders of magnitude shorter than  $\tau_m$ , the exciton itself cannot be the magnetically enhanced state, but rather must give rise to the latter during its recombination as a long-lived intermediate state.

The long lifetime of excitons in  $\text{CrCl}_3$  should promote nonradiative recombination. In Fig. 4e, we display the PL intensity normalized by the number of layers at 730 nm excitation ( $X_1$ ) for several  $\text{CrCl}_3$  regions between 2 to 11 layers thick. The red (blue) data points denote regions encapsulated (not encapsulated) by hBN, where both samples were prepared in the glovebox and simultaneously loaded into the cryostat. Although we observe variations among regions of identical thickness, the PL *per layer* for both conditions decreases for thinner flakes, a trend similar to  $\text{CrI}_3$  [4]. Simultaneously, the exciton lifetime  $\tau_{opt}$  is reduced with decreasing thickness (Fig. 4f), with flakes lacking hBN encapsulation having shorter lifetimes and lower PL for comparable thickness. Taken together, Figs. 4e,f clearly identify the rise

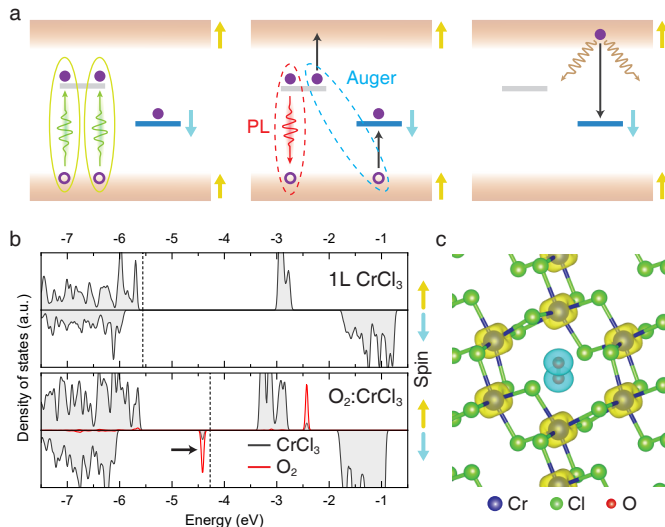


FIG. 5. Magnetization enhancement through defect-assisted Auger recombination. (a) Mechanism. Left: near-resonant excitation of CrCl<sub>3</sub> creates strongly bound excitons (filled circle - electron, open circle - hole). An in-gap defect state is occupied. Center: Excitons can recombine radiatively, resulting in PL (red), or nonradiatively through defect-assisted Auger recombination (blue). The Auger process converts a spin-down defect electron into a spin-up CrCl<sub>3</sub> conduction electron. Right: the excited state after Auger recombination decays by multi-phonon emission and electron capture by the ionized defect. (b) Spin-resolved density of states for a pristine CrCl<sub>3</sub> monolayer (top) and a CrCl<sub>3</sub> monolayer with adsorbed O<sub>2</sub> molecules (bottom). Gray (red) lines indicate the contributions from monolayer CrCl<sub>3</sub> (O<sub>2</sub>). The Fermi level is shown as the vertical dashed line. (c) Spatial spin distribution for monolayer CrCl<sub>3</sub> near an O<sub>2</sub> adsorbate. The spin-down density (cyan) is contributed by the O<sub>2</sub>-derived in-gap state marked by the black arrow in b).

of nonradiative transitions, as opposed to diminishing radiative oscillator strength, as the primary mechanism for PL quenching in thinner layers.

Our evidence that exciton pumping creates an alternative magnetically enhanced electronic state hints that the energy dissipated in nonradiative exciton recombination may be transferred to a nearby electronic carrier, a channel known as Auger recombination. Moreover, the sensitivity of  $\tau_{opt}$  to layer thickness and surface encapsulation (Fig. 4f) implies that Auger recombination in CrCl<sub>3</sub> is catalyzed by defects residing predominantly in the surface layers. Excitons produced in the bulk can hop between layers [44] within a finite diffusion length to reach the surface, where the recombination rate is highest.

### E. Surface Adsorbate Mechanism

We thus propose the following defect-assisted Auger mechanism [21, 22] to explain the optically-enhanced

magnetization in atomically thin CrCl<sub>3</sub>. Auger recombination of excitons is mediated by an occupied mid-gap level, which captures the hole of the exciton and transfers the excess energy to its electron partner, injecting it into the spin-polarized conduction band (Fig. 5a, middle). The rate for this three-particle scattering crucially hinges on the probability of finding the exciton's electron and hole near each other, and hence should be strongly enhanced in CrCl<sub>3</sub> with its near-atomic exciton radii [21, 22]. The conventional Auger process for delocalized Wannier-Mott excitons in narrow bandgap semiconductors is instead governed by exciton-exciton collisions, resulting in an exciton lifetime that is inversely proportional to the square of the exciton density in the high-density limit [45]. In contrast, Fig. 4g shows that the lifetime  $\tau_{opt}$  in few-layer CrCl<sub>3</sub> is virtually independent of the optical excitation power, assumed to be proportional to the exciton density. This independence is a direct signature of defect-assisted Auger recombination of localized excitons [21, 22].

The resulting excited state persists until the ionized defect level recaptures an electron from the conduction band (Fig. 5a, right), which must be accompanied by multi-phonon emission and results in the slow magnetization recovery time  $\tau_m$  observed at cryogenic temperatures. For monolayer CrCl<sub>3</sub>, electron doping via halogen vacancies [23, 25] or metal adsorption [26, 27] has indeed been proposed to increase the electron charge (from  $3d^3$  to  $3d^4$ ) and magnetic moment of the Cr ion, which adopts a high spin configuration in the weak halogen ligand field. In the band picture, this amounts to partial filling of the lowest energy, majority-spin conduction bands contributed by the Cr  $e_g$  orbitals. Remarkably, we realize this doping effect for few-layer CrCl<sub>3</sub> in an optically controlled manner, providing a direct on-off contrast that is vital to its detection.

To determine the most likely impurity that mediates exciton recombination, we turn to DFT calculations. Surface-sensitive probes have determined that the most prevalent defects in few layer CrCl<sub>3</sub> are Cl vacancies and oxygen-related impurities [46, 47]. Since our PL data indicate a surface recombination center whose density is affected by encapsulation (Figs. 4e,f), we focus our attention to oxygen impurities that are nevertheless formed during our experimental process. Figure 5b displays the spin-resolved, projected density of states calculated for a CrCl<sub>3</sub> monolayer with O<sub>2</sub> molecules adsorbed at the hollow center of the Cr honeycomb rings. Free O<sub>2</sub> molecules carry a magnetic moment of  $2\mu_B$  due to two unpaired electrons in their degenerate  $\pi^*$  orbitals. We find that the O<sub>2</sub> adsorbate in CrCl<sub>3</sub> introduces an occupied mid-gap state with a spin density opposite to that of the CrCl<sub>3</sub> monolayer (Fig. 5c). This ferrimagnetic ordering of O<sub>2</sub> and Cr moments is favored by 59 meV over parallel alignment in our DFT results (see Supplementary Section VII for calculations of additional forms of oxygen impurities).

For perfect spin polarization, Auger recombination converts a spin-down oxygen electron into a spin-up con-

duction electron, increasing the system magnetization by  $2\mu_B$  per electron. For adsorbates, the surface layers of  $\text{CrCl}_3$  should dominate the contribution to the optical magnetization enhancement. This naturally produces an even-odd effect, since in odd-layer (even-layer) regions, the top and bottom layers have parallel (anti-parallel) magnetizations.

Experimental evidence for a surface-dominated enhancement is provided by two measurements. First, for the 6/8-layer stripe of Fig. 1 at high  $B_{ext}$ , we observe a dc stray field that is approximately twice as strong as its neighboring odd-layer regions (Fig. 1e), indicating an extra flipped layer in its volume. However, its transient stray field under exciton pumping is virtually identical in strength to the nearby odd-layer regions (Hahn map, Fig. 6a). This is explained if the surface monolayers dominate the contribution to the optical enhancement since if all layers contributed equally, the transient signal would be instead twice as strong. Indeed, the flipped layer in the 6/8-layer stripe is expected to be a surface layer, since this configuration minimizes the energy penalty for breaking AF interlayer exchange.

Second, we fabricate another  $\text{CrCl}_3$  flake where we deliberately encapsulate only a portion of the flake with hBN. This allows an unequivocal comparison of the surface condition by ensuring that the same starting sample experiences identical exposure times to oxygen both inside the glovebox and in ambient during sample loading. In Fig. 6b, we plot the PL of the  $\text{CrCl}_3$  flake on diamond using a logarithmic colorbar to emphasize thinner regions. Areas of the same layer thickness are significantly dimmer when not encapsulated by hBN, corroborating the role of surface defects in promoting nonradiative exciton recombination (Fig. 4e,f.).

Figure 6c displays the static stray field ( $B_{NV}$ ) image of the same flake, showing that antiferromagnetic interlayer coupling is retained down to three layers. The weak edge of positive dc field (orange) observed at the hBN boundary suggests a small reduction in the dc magnetization for the exposed portion; however, this distinction is limited by the sensitivity of the dc measurement. On the other hand, the transient stray field image obtained under exciton pumping with the single green beam displays a prominent contrast between the two conditions (Fig. 6d). The average Hahn echo phase  $\Phi$  recorded over the exposed portion of the odd-layer stripes increases by more than a factor of two over the hBN covered portion ( $\Phi_{exposed} \approx 0.60$  rad,  $\Phi_{covered} \approx 0.25$  rad), excluding a transitional region near the termination of the hBN. This comparison pinpoints environmentally-induced defects in the surface layers as the common catalyst for optically-enhanced magnetization and nonradiative exciton recombination.

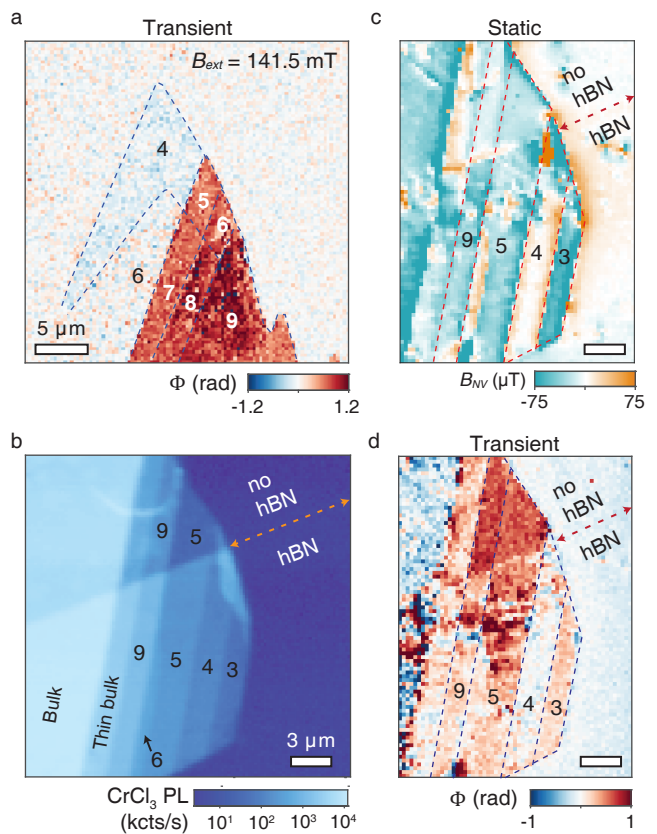


FIG. 6. Surface-sensitive magnetization enhancement. (a) Hahn image for the 4-9 layer  $\text{CrCl}_3$  flake (hBN encapsulated) of Fig. 1 at high  $B_{ext} = 141.5$  mT. The Hahn precession angle  $\Phi$  with  $2\tau = 13$   $\mu\text{s}$  is measured as the single green beam (515 nm) is rastered over the flake. The amplitude of the transient field over the 6/8-layer stripe is similar to the neighboring odd-layer regions even though the former possesses a twice larger volume magnetization. (b) PL image ( $>800$  nm) for a 3-9 layer  $\text{CrCl}_3$  flake with deliberate partial hBN encapsulation. The edge of the hBN cuts across the entire flake parallel to the dashed orange line. The PL is quenched over unencapsulated regions due to defect-assisted, nonradiative exciton recombination. (c) Static stray field ( $B_{NV}$ ) image of the same flake confirming even-odd layer parity and displaying marginally reduced stray fields over the hBN unencapsulated area. (d) Hahn image of the same flake with  $2\tau = 19$   $\mu\text{s}$ . The transient stray field, proportional to  $\Phi$ , exhibits a clear delineation between the exposed and covered areas of the odd-layer stripes, demonstrating that the degree of surface oxidation controls the magnitude of the optical magnetization enhancement.

## F. Conclusions

We have revealed that exciton pumping enhances the in-plane, layer-alternating magnetization of atomically-thin  $\text{CrCl}_3$ . Experimental and theoretical evidences thoroughly support a mechanism where the Auger recombination of strongly bound excitons in the surface monolayers activates charge transfer between oxygen-induced



defects and the Cr majority-spin bands. Through an innovative quantum coherent sensing protocol, our work unambiguously demonstrates that impurities can modulate intrinsic magnetism in single atomic layers [23–28]. The revealed exciton-mediated charge transfer may be applicable to diverse semiconducting 2D magnets, including intrinsic Cr- and Mn-based compounds and magnetically-doped TMDs, where long-range order in the latter are still under debate. These systems, including CrX<sub>3</sub> [7, 8, 13–15], CrPS<sub>4</sub> [48], MnPX<sub>3</sub> [49], Fe-doped MoS<sub>2</sub> [50] and V-doped WSe<sub>2</sub> monolayers [51], all harbor tightly bound excitons, either due to nearly forbidden *d-d* transitions or to reduced dielectric screening, and are susceptible to deep-level states due to oxidization or native defects. Indeed, our study opens diverse strategies for future efforts to optimize the magnetization enhancement and access the predicted increases in Néel or Curie tem-

peratures by systematic surface dosing or by extending to bulk layers via doping, intercalation, or defect creation through irradiation.

Optical control is furthermore attractive as a high-bandwidth knob to modulate the resonant coupling between 2D spin ensembles and small mode volume superconducting resonators for solid-state quantum memory applications [52, 53]. Conventionally achieved by pulsing an external magnetic flux, tuning the magnon resonances and microwave resonator in and out of match could alternatively be realized with fast and focusable pulses of light that change the magnetization and internal field of the 2D spin ensemble [54, 55]. Finally, the developed pump-probe quantum sensing technique with its unique combination of sensitivity and spatiotemporal resolution opens a promising new window into optically-controlled magnetism in van der Waals systems.

- 
- [1] B. Huang, G. Clark, E. Navarro-Moratalla, D. R. Klein, R. Cheng, K. L. Seyler, D. Zhong, E. Schmidgall, M. A. McGuire, D. H. Cobden, W. Yao, D. Xiao, P. Jarillo-Herrero, and X. Xu, Layer-dependent ferromagnetism in a van der Waals crystal down to the monolayer limit, *Nature* **546**, 270 (2017).
- [2] C. Gong, L. Li, Z. Li, H. Ji, A. Stern, Y. Xia, T. Cao, W. Bao, C. Wang, Y. Wang, Z. Q. Qiu, R. J. Cava, S. G. Louie, J. Xia, and X. Zhang, Discovery of intrinsic ferromagnetism in two-dimensional van der Waals crystals, *Nature* **546**, 265 (2017).
- [3] Z. Zhang, J. Shang, C. Jiang, A. Rasmita, W. Gao, and T. Yu, Direct Photoluminescence Probing of Ferromagnetism in Monolayer Two-Dimensional CrBr<sub>3</sub>, *Nano Letters* **19**, 3138 (2019).
- [4] K. L. Seyler, D. Zhong, D. R. Klein, S. Gao, X. Zhang, B. Huang, E. Navarro-Moratalla, L. Yang, D. H. Cobden, M. A. McGuire, W. Yao, D. Xiao, P. Jarillo-Herrero, and X. Xu, Ligand-field helical luminescence in a 2D ferromagnetic insulator, *Nature Physics* **14**, 277 (2018).
- [5] X. Wang, J. Cao, Z. Lu, A. Cohen, H. Kitadai, T. Li, Q. Tan, M. Wilson, C. H. Lui, D. Smirnov, S. Sharifzadeh, and X. Ling, Spin-induced linear polarization of photoluminescence in antiferromagnetic van der Waals crystals, *Nature Materials* **20**, 964 (2021).
- [6] N. P. Wilson, K. Lee, J. Cenker, K. Xie, A. H. Dismukes, E. J. Telford, J. Fonseca, S. Sivakumar, C. Dean, T. Cao, X. Roy, X. Xu, and X. Zhu, Interlayer electronic coupling on demand in a 2D magnetic semiconductor, *Nature Materials* **20**, 1657 (2021).
- [7] M. Wu, Z. Li, T. Cao, and S. G. Louie, Physical origin of giant excitonic and magneto-optical responses in two-dimensional ferromagnetic insulators, *Nature Communications* **10**, 2371 (2019).
- [8] A. Molina-Sánchez, G. Catarina, D. Sangalli, and J. Fernández-Rossier, Magneto-optical response of chromium trihalide monolayers: chemical trends, *Journal of Materials Chemistry C* **8**, 8856 (2020).
- [9] J. Choi, C. Lane, J.-X. Zhu, and S. A. Crooker, Asymmetric magnetic proximity interactions in MoSe<sub>2</sub>/CrBr<sub>3</sub> van der Waals heterostructures, *Nature Materials* **22**, 305 (2023).
- [10] V. Ortiz Jimenez, Y. T. H. Pham, M. Liu, F. Zhang, Z. Yu, V. Kalappattil, B. Muchharla, T. Eggers, D. L. Duong, M. Terrones, and M. Phan, Light-Controlled Room Temperature Ferromagnetism in Vanadium-Doped Tungsten Disulfide Semiconducting Monolayers, *Advanced Electronic Materials* **7**, 2100030 (2021).
- [11] P. Zhang, T.-F. Chung, Q. Li, S. Wang, Q. Wang, W. L. B. Huey, S. Yang, J. E. Goldberger, J. Yao, and X. Zhang, All-optical switching of magnetization in atomically thin CrI<sub>3</sub>, *Nature Materials* **21**, 1373 (2022).
- [12] X. Wang, C. Xiao, H. Park, J. Zhu, C. Wang, T. Taniguchi, K. Watanabe, J. Yan, D. Xiao, D. R. Gamelin, W. Yao, and X. Xu, Light-induced ferromagnetism in moiré superlattices, *Nature* **604**, 468 (2022).
- [13] M. Wu, Z. Li, and S. G. Louie, Optical and magneto-optical properties of ferromagnetic monolayer CrBr<sub>3</sub>: A first-principles GW and GW plus Bethe-Salpeter equation study, *Physical Review Materials* **6**, 014008 (2022).
- [14] L. Zhu and L. Yang, Quasiparticle energies and excitonic effects of chromium trichloride: From two dimensions to bulk, *Physical Review B* **101**, 245401 (2020).
- [15] S. Acharya, D. Pashov, A. N. Rudenko, M. Rösner, M. van Schilfgaarde, and M. I. Katsnelson, Real- and momentum-space description of the excitons in bulk and monolayer chromium tri-halides, *npj 2D Materials and Applications* **6**, 33 (2022).
- [16] G. Wang, A. Chernikov, M. M. Glazov, T. F. Heinz, X. Marie, T. Amand, and B. Urbaszek, Colloquium : Excitons in atomically thin transition metal dichalcogenides, *Reviews of Modern Physics* **90**, 021001 (2018).
- [17] N. Shimamoto, S.-i. Ohkoshi, O. Sato, and K. Hashimoto, Control of Charge-Transfer-Induced Spin Transition Temperature on Cobalt-Iron Prussian Blue Analogues, *Inorganic Chemistry* **41**, 678 (2002).
- [18] V. Pinchetti, Q. Di, M. Lorenzon, A. Camellini, M. Fasoli, M. Zavelani-Rossi, F. Meinardi, J. Zhang, S. A. Crooker, and S. Brovelli, Excitonic pathway to photoinduced magnetism in colloidal nanocrystals with nonmagnetic dopants, *Nature Nanotechnology* **13**, 145 (2018).
- [19] R. V. Mikhaylovskiy, T. J. Huisman, V. A. Gavrichkov,

- S. I. Polukeev, S. G. Ovchinnikov, D. Afanasiev, R. V. Pisarev, T. Rasing, and A. V. Kimel, Resonant Pumping of d-d Crystal Field Electronic Transitions as a Mechanism of Ultrafast Optical Control of the Exchange Interactions in Iron Oxides, *Physical Review Letters* **125**, 157201 (2020).
- [20] A. Ron, S. Chaudhary, G. Zhang, H. Ning, E. Zoghlin, S. D. Wilson, R. D. Averitt, G. Refael, and D. Hsieh, Ultrafast Enhancement of Ferromagnetic Spin Exchange Induced by Ligand-to-Metal Charge Transfer, *Physical Review Letters* **125**, 197203 (2020).
- [21] C.-H. Chen and H.-F. Meng, Defect Auger exciton dissociation and impact ionization in conjugated polymers, *Physical Review B* **64**, 125202 (2001).
- [22] H. Wang, J. H. Strait, C. Zhang, W. Chan, C. Manolatos, S. Tiwari, and F. Rana, Fast exciton annihilation by capture of electrons or holes by defects via Auger scattering in monolayer metal dichalcogenides, *Physical Review B* **91**, 165411 (2015).
- [23] Y. Zhao, L. Lin, Q. Zhou, Y. Li, S. Yuan, Q. Chen, S. Dong, and J. Wang, Surface Vacancy-Induced Switchable Electric Polarization and Enhanced Ferromagnetism in Monolayer Metal Trihalides, *Nano Letters* **18**, 2943 (2018).
- [24] C. Wang, X. Zhou, Y. Pan, J. Qiao, X. Kong, C.-C. Kaun, and W. Ji, Layer and doping tunable ferromagnetic order in two-dimensional CrS<sub>2</sub> layers, *Physical Review B* **97**, 245409 (2018).
- [25] M. Pizzochero, Atomic-scale defects in the two-dimensional ferromagnet CrI<sub>3</sub> from first principles, *Journal of Physics D: Applied Physics* **53**, 244003 (2020).
- [26] Y. Guo, S. Yuan, B. Wang, L. Shi, and J. Wang, Half-metallicity and enhanced ferromagnetism in Li-adsorbed ultrathin chromium triiodide, *Journal of Materials Chemistry C* **6**, 5716 (2018).
- [27] Q. Yang, X. Hu, X. Shen, A. V. Krasheninnikov, Z. Chen, and L. Sun, Enhancing Ferromagnetism and Tuning Electronic Properties of CrI<sub>3</sub> Monolayers by Adsorption of Transition-Metal Atoms, *ACS Applied Materials and Interfaces* **13**, 21593 (2021).
- [28] M. Luo, Y. Li, K. Wang, and Y. Shen, Adsorption induced magnetic anisotropy in the two-dimensional magnet CrCl<sub>3</sub>, *Solid State Communications* **321**, 114048 (2020).
- [29] M. A. McGuire, G. Clark, S. KC, W. M. Chance, G. E. Jellison, V. R. Cooper, X. Xu, and B. C. Sales, Magnetic behavior and spin-lattice coupling in cleavable van der Waals layered CrCl<sub>3</sub> crystals, *Physical Review Materials* **1**, 014001 (2017).
- [30] X. Cai, T. Song, N. P. Wilson, G. Clark, M. He, X. Zhang, T. Taniguchi, K. Watanabe, W. Yao, D. Xiao, M. A. McGuire, D. H. Cobden, and X. Xu, Atomically Thin CrCl<sub>3</sub>: An In-Plane Layered Antiferromagnetic Insulator, *Nano Letters* **19**, 3993 (2019).
- [31] Z. Wang, M. Gibertini, D. Dumcenco, T. Taniguchi, K. Watanabe, E. Giannini, and A. F. Morpurgo, Determining the phase diagram of atomically thin layered antiferromagnet CrCl<sub>3</sub>, *Nature Nanotechnology* **14**, 1116 (2019).
- [32] D. R. Klein, D. MacNeill, Q. Song, D. T. Larson, S. Fang, M. Xu, R. A. Ribeiro, P. C. Canfield, E. Kaxiras, R. Comin, and P. Jarillo-Herrero, Enhancement of interlayer exchange in an ultrathin two-dimensional magnet, *Nature Physics* **15**, 1255 (2019).
- [33] H. H. Kim, B. Yang, S. Li, S. Jiang, C. Jin, Z. Tao, G. Nichols, F. Sfigakis, S. Zhong, C. Li, S. Tian, D. G. Cory, G.-X. Miao, J. Shan, K. F. Mak, H. Lei, K. Sun, L. Zhao, and A. W. Tsien, Evolution of interlayer and intralayer magnetism in three atomically thin chromium trihalides, *Proceedings of the National Academy of Sciences* **116**, 11131 (2019).
- [34] A. Bedoya-Pinto, J.-r. Ji, A. K. Pandeya, P. Gargiani, M. Valvidares, P. Sessi, J. M. Taylor, F. Radu, K. Chang, and S. S. P. Parkin, Intrinsic 2D-XY ferromagnetism in a van der Waals monolayer, *Science* **374**, 616 (2021).
- [35] L. Thiel, Z. Wang, M. A. Tschudin, D. Rohner, I. Gutiérrez-Lezama, N. Ubrig, M. Gibertini, E. Giannini, A. F. Morpurgo, and P. Maletinsky, Probing magnetism in 2D materials at the nanoscale with single-spin microscopy, *Science* **364**, 973 (2019).
- [36] Q.-C. Sun, T. Song, E. Anderson, A. Brunner, J. Förster, T. Shalomayeva, T. Taniguchi, K. Watanabe, J. Gräfe, R. Stöhr, X. Xu, and J. Wrachtrup, Magnetic domains and domain wall pinning in atomically thin CrBr<sub>3</sub> revealed by nanoscale imaging, *Nature Communications* **12**, 1989 (2021).
- [37] T. Song, Q.-C. Sun, E. Anderson, C. Wang, J. Qian, T. Taniguchi, K. Watanabe, M. A. McGuire, R. Stöhr, D. Xiao, T. Cao, J. Wrachtrup, and X. Xu, Direct visualization of magnetic domains and moiré magnetism in twisted 2D magnets, *Science* **374**, 1140 (2021).
- [38] X.-Y. Zhang, Y.-X. Wang, T. A. Tartaglia, T. Ding, M. J. Gray, K. S. Burch, F. Tafti, and B. B. Zhou, ac Susceptometry of 2D van der Waals Magnets Enabled by the Coherent Control of Quantum Sensors, *PRX Quantum* **2**, 030352 (2021).
- [39] Y.-X. Wang, X.-Y. Zhang, C. Li, X. Yao, R. Duan, T. K. M. Graham, Z. Liu, F. Tafti, D. Broido, Y. Ran, and B. B. Zhou, Visualization of bulk and edge photocurrent flow in anisotropic Weyl semimetals, *Nature Physics* **19**, 507 (2023).
- [40] F. Fabre, A. Finco, A. Purbawati, A. Hadj-Azzem, N. Rougemaille, J. Coraux, I. Philip, and V. Jacques, Characterization of room-temperature in-plane magnetization in thin flakes of CrTe<sub>2</sub> with a single-spin magnetometer, *Physical Review Materials* **5**, 034008 (2021).
- [41] V. M. Bermudez and D. S. McClure, Spectroscopic studies of the two-dimensional magnetic insulators chromium trichloride and chromium tribromide-I, *Journal of Physics and Chemistry of Solids* **40**, 129 (1979).
- [42] B. B. Zhou, P. C. Jerger, K.-H. Lee, M. Fukami, F. Mujid, J. Park, and D. D. Awschalom, Spatiotemporal Mapping of a Photocurrent Vortex in Monolayer MoS<sub>2</sub> Using Diamond Quantum Sensors, *Physical Review X* **10**, 011003 (2020).
- [43] D. A. Wahab, M. Augustin, S. M. Valero, W. Kuang, S. Jenkins, E. Coronado, I. V. Grigorieva, I. J. Vera-Marun, E. Navarro-Moratalla, R. F. L. Evans, K. S. Novoselov, and E. J. G. Santos, Quantum Rescaling, Domain Metastability, and Hybrid Domain-Walls in 2D CrI<sub>3</sub> Magnets, *Advanced Materials* **33**, 2004138 (2021).
- [44] N. S. Ginsberg and W. A. Tisdale, Spatially Resolved Photogenerated Exciton and Charge Transport in Emerging Semiconductors, *Annual Review of Physical Chemistry* **71**, 1 (2020).
- [45] A. McAllister, D. Bayerl, and E. Kioupakis, Radiative and Auger recombination processes in indium nitride, *Applied Physics Letters* **112**, 251108 (2018).

- [46] D. Mastrrippolito, L. Ottaviano, J. Wang, J. Yang, F. Gao, M. Ali, G. D'Olimpio, A. Politano, S. Palleschi, S. Kazim, R. Gunnella, A. Di Cicco, A. Sgarlata, J. Strychalska-Nowak, T. Klimczuk, R. J. Cava, L. Lozzi, and G. Profeta, Emerging oxidized and defective phases in low-dimensional CrCl<sub>3</sub>, *Nanoscale Advances* **3**, 4756 (2021).
- [47] D. Mastrrippolito, J. Wang, G. Profeta, and L. Ottaviano, Unconventional ferrimagnetism and enhanced magnetic ordering temperature in monolayer CrCl<sub>3</sub> by introducing O impurities and Cl vacancies, *Journal of Physics: Materials* **5**, 014004 (2022).
- [48] S. Kim, S. Yoon, H. Ahn, G. Jin, H. Kim, M.-H. Jo, C. Lee, J. Kim, and S. Ryu, Photoluminescence Path Bifurcations by Spin Flip in Two-Dimensional CrPS<sub>4</sub>, *ACS Nano* **16**, 16385 (2022).
- [49] M. Birowska, P. E. Faria Junior, J. Fabian, and J. Kuntstmann, Large exciton binding energies in MnPS<sub>3</sub> as a case study of a van der Waals layered magnet, *Physical Review B* **103**, L121108 (2021).
- [50] S. Fu, K. Kang, K. Shayan, A. Yoshimura, S. Dadras, X. Wang, L. Zhang, S. Chen, N. Liu, A. Jindal, X. Li, A. N. Pasupathy, A. N. Vamivakas, V. Meunier, S. Strauf, and E.-H. Yang, Enabling room temperature ferromagnetism in monolayer MoS<sub>2</sub> via in situ iron-doping, *Nature Communications* **11**, 2034 (2020).
- [51] L.-A. T. Nguyen, K. P. Dhakal, Y. Lee, W. Choi, T. D. Nguyen, C. Hong, D. H. Luong, Y.-M. Kim, J. Kim, M. Lee, T. Choi, A. J. Heinrich, J.-H. Kim, D. Lee, D. L. Duong, and Y. H. Lee, Spin-Selective Hole-Exciton Coupling in a V-Doped WSe<sub>2</sub> Ferromagnetic Semiconductor at Room Temperature, *ACS Nano* **15**, 20267 (2021).
- [52] C. W. Zollitsch, S. Khan, V. T. T. Nam, I. A. Verzhbitskiy, D. Sagkovits, J. O'Sullivan, O. W. Kennedy, M. Strungaru, E. J. G. Santos, J. J. L. Morton, G. Eda, and H. Kurebayashi, Probing spin dynamics of ultra-thin van der Waals magnets via photon-magnon coupling, *Nature Communications* **14**, 2619 (2023).
- [53] Y. Kubo, C. Grezes, A. Dewes, T. Umeda, J. Isoya, H. Sumiya, N. Morishita, H. Abe, S. Onoda, T. Ohshima, V. Jacques, A. Dréau, J.-F. Roch, I. Diniz, A. Auffeves, D. Vion, D. Esteve, and P. Bertet, Hybrid Quantum Circuit with a Superconducting Qubit Coupled to a Spin Ensemble, *Physical Review Letters* **107**, 220501 (2011).
- [54] D. MacNeill, J. T. Hou, D. R. Klein, P. Zhang, P. Jarillo-Herrero, and L. Liu, Gigahertz Frequency Antiferromagnetic Resonance and Strong Magnon-Magnon Coupling in the Layered Crystal CrCl<sub>3</sub>, *Physical Review Letters* **123**, 047204 (2019).
- [55] S. R. Singamaneni, L. M. Martinez, J. Niklas, O. G. Poluektov, R. Yadav, M. Pizzochero, O. V. Yazyev, and M. A. McGuire, Light induced electron spin resonance properties of van der Waals CrX<sub>3</sub> (X = Cl, I) crystals, *Applied Physics Letters* **117**, 082406 (2020).
- [56] A. Zalic, S. Simon, S. Remennik, A. Vakahi, G. D. Gu, and H. Steinberg, FeTe<sub>0.55</sub>Se<sub>0.45</sub> van der Waals tunneling devices, *Physical Review B* **100**, 064517 (2019).
- [57] G. Kresse and D. Joubert, From ultrasoft pseudopotentials to the projector augmented-wave method, *Physical Review B* **59**, 1758 (1999).
- [58] Y. Yekta, H. Hadipour, E. Şaşıoğlu, C. Friedrich, S. A. Jafari, S. Blügel, and I. Mertig, Strength of effective Coulomb interaction in two-dimensional transition-metal halides MX<sub>2</sub> and MX<sub>3</sub> (M = Ti, V, Cr, Mn, Fe, Co, Ni; X = Cl, Br, I), *Physical Review Materials* **5**, 034001 (2021).
- [59] S. L. Dudarev, G. A. Botton, S. Y. Savrasov, C. J. Humphreys, and A. P. Sutton, Electron-energy-loss spectra and the structural stability of nickel oxide: An LSDA+U study, *Physical Review B* **57**, 1505 (1998).

## I. APPENDIX A: SAMPLE DETAILS

The experimental results have been verified on multiple CrCl<sub>3</sub> crystals grown by two different academic groups and by a commercial vendor (2D Semiconductors; Fig. 4). For Figs. 1-3, the CrCl<sub>3</sub> crystals were synthesized by vacuum sublimation of chromium (III) chloride powder (99.9%) in a single-zone tube furnace. The powder material with a total mass of 500 mg was sealed inside an evacuated silica tube, which was transferred into the furnace and heated to 650 °C at 5 °C/min, kept at that temperature for 72 hours, and cooled to room temperature. Large crystals of CrCl<sub>3</sub> with millimeter-size lateral dimensions and micron-size thickness was obtained. For Fig. 6, the partially hBN-encapsulated CrCl<sub>3</sub> crystal was synthesized by vacuum sublimation of chromium (III) chloride powder (99.9%, Strem, USA) in a two zone tube furnace in a quartz ampoule. 25 g of CrCl<sub>3</sub> were placed in an ampoule (50x250 mm) and melt sealed under high vacuum of diffusion pump with liquid nitrogen cold trap at pressure under 1x10<sup>-3</sup> Pa. The sealed ampoule was placed in two zone horizontal furnace. First the growth zone was heated on 700 °C, while the source zone was kept at 500 °C. After two days the thermal gradient was reversed and source zone was kept at 700 °C while the growth zone temperature was slowly reduced from 680 to 600 °C over a period of one week and for additional one week was kept at 600 °C. Over 90% of the material was transported forming plate crystals with size up to 30 mm and thickness under 0.1 mm.

Two diamond substrates are used in this work, both containing 200±133 nm of <sup>12</sup>C isotopically-purified diamond (>99.995% <sup>12</sup>C as per secondary ion mass spectrometry characterization). Pre-growth, these electronic grade bulk diamond substrates (Element Six) were fine-polished (Syntek) down to ≤0.3 nm root mean square (RMS) surface roughness. Thereafter, they underwent a cycling inductively coupled plasma-reactive ion etch (ICP-RIE) to remove the polish-induced damage (five cycles of Ar 25 sccm, Cl<sub>2</sub> 40 sccm, 10 mTorr, 400 W ICP, 200 W bias and O<sub>2</sub> 50 sccm, 10 mTorr, 700 W ICP, 100 W bias). The ICP-RIE process resulted in ≈2.5 μm removal while maintaining ≤ 0.3 nm RMS. This was followed by a multi-step annealing process at <2·10<sup>-6</sup> Torr (1.6 °C/min ramp, 12 h at 200 °C, 8 h at 400 °C, 8 h at 850 °C, and 2 h at 1200 °C). Overgrowth was performed in a custom-configured microwave plasma chemical vapor deposition system (SEKI DIAMOND SDS6350) at 11.5 W/mm<sup>2</sup>, 0.2:400 sccm <sup>12</sup>CH<sub>4</sub>:H<sub>2</sub>, and maintained at ≈850 °C and 25 Torr. Both the hydrogen and the methane were purified to better than 8 and 6 “nines”,

respectively, with the chamber being pumped down to  $<5 \cdot 10^{-8}$  Torr base pressure before growth. Before the introduction of the methane precursor, the hydrogen plasma was allowed to run for 20 min as to etch away any residual surface carbonaceous contaminants.

To create a shallow layer of NV centers, one diamond sample was implanted with 40 keV  $^{14}\text{N}$  ions at  $10^{12}$  ions/cm<sup>2</sup> and annealed at 1050 °C in forming gas (5% H<sub>2</sub>, 95% Ar) for two hours, while the other was implanted with 45 keV  $^{15}\text{N}$  ions  $10^{12}$  ions/cm<sup>2</sup> and annealed at 1050 °C for three hours. At  $B_{ext} = 141.5$  mT, the average Ramsey  $T_2^*$  coherence time on the bare diamond is 3  $\mu\text{s}$  and the average Hahn echo  $T_2$  coherence time is 80  $\mu\text{s}$ . This  $T_2^*$  is a factor of ten longer than similar ensemble samples in non-isotopically purified diamond.

CrCl<sub>3</sub> and hBN flakes are exfoliated onto separate polydimethylsiloxane (PDMS) stamps using blue tape (Ultron 1009R) inside an argon-filled glovebox with nominal residual concentrations of O<sub>2</sub> and H<sub>2</sub>O  $<0.01$  ppm. Air-sensitive atomically thin samples are known to still undergo chemical reactions inside a glovebox, despite impurity gas concentrations beneath the detection limit of standard analyzers [56]. A few-layer CrCl<sub>3</sub> flake is then identified by optical contrast (Supplementary Section II). The target CrCl<sub>3</sub> flake is transferred onto the diamond substrate and encapsulated by a suitable hBN flake using sequential PDMS viscoelastic transfer at room temperature. The diamond substrate is taken out of the glovebox, mounted onto a sample holder, and loaded into a closed-cycle optical cryostat (Montana Instruments) for pump-out and cool-down in less than 30 minutes.

## II. APPENDIX B: NV CENTER MEASUREMENTS

NV magnetic imaging is performed in a custom-built, dual-beam cryogenic (4 K) confocal microscope by pixel-to-pixel scanning of a diffraction-limited probe beam (FWHM = 400 nm). Full details of the optical and electronic setup are provided in Supplementary Section III. Due to the long  $T_2^*$  in our isotopically purified diamond samples, we can use pulsed ODMR sequences with a long 800 ns  $\pi$ -pulse resonant with the  $|m_s = 0\rangle \rightarrow |m_s = -1\rangle$  spin transition. Pulsed ODMR resolves the nitrogen hyperfine splitting and enhances the dc field ( $B_{NV}$ ) sensitivity, but requires more data points per pixel (e.g., 25 frequency points to sample the triply-split  $^{14}\text{N}$  resonance lineshape). For Hahn ( $\Phi$ ) imaging, we acquire four data points per pixel corresponding to four different phases for the final  $\pi/2$  projection pulse (30 ns width):  $X_{\pm\pi/2}$  and  $Y_{\pm\pi/2}$ , where the denoted  $X$ - and  $Y$ -axis Bloch sphere rotations are realized by in-phase (I) and quadrature (Q) modulation of the microwave drive. The  $X_P$  and  $Y_P$  projections are then determined differentially by  $X_P =$

$C(X_{-\pi/2}) - C(X_{+\pi/2})$  and  $Y_P = C(Y_{-\pi/2}) - C(Y_{+\pi/2})$ , where  $C$  denotes the integrated photon counts, and then normalized to the range  $\pm 1$  by the Rabi contrast.

## III. APPENDIX C: DENSITY FUNCTIONAL THEORY CALCULATIONS

Spin-polarized DFT calculations are performed using the Vienna *Ab initio* Simulation Package (VASP) within the projector augmented wave method [57]. The van der Waals interaction with impurity molecules is described by the exchange-correlation functional in the generalized gradient approximation as parameterized by Perdew-Burke-Ernzerhof and DFT+D3 method. The correlation effect is modeled by  $U_{\text{eff}} = 3.5$  eV on the Cr 3d electrons [58] for the DFT+U scheme formulated by Dudarev [59]. The kinetic energy cut-off is set to 400 eV. The Brillouin zone is sampled by a two-dimensional  $\Gamma$ -centered  $k$ -point mesh with  $\sim 0.09$  Å intervals, i.e.  $12 \times 12 \times 1$  for a monolayer CrCl<sub>3</sub> primitive cell. Electronic energy convergence is performed until an accuracy of  $10^{-7}$  eV. Lattice and ionic relaxation are carried out until the Hellmann-Feynman forces acting on each ion are reduced below 0.01 eV/Å.

## IV. ACKNOWLEDGMENTS

The authors thank B. Flebus for valuable discussions. B.B.Z. acknowledges the National Science Foundation (NSF) CAREER award No. DMR-2047214 and NSF award No. ECCS-2041779. This material is based on work supported by the Air Force Office of Scientific Research under award no. FA2386-21-1-4095. B.Y. acknowledges the financial support by the European Research Council (ERC Consolidator Grant “NonlinearTopo”, No. 815869) and the ISF - Personal Research Grant (No. 2932/21). The diamond synthesis work was primarily supported by the U.S. Department of Energy, Office of Basic Energy Sciences, Materials Science and Engineering Division (N.D., D.D.A., F.J.H.). F.T. acknowledges support from the U.S. Department of Energy, Office of Basic Energy Sciences, Division of Physical Behavior of Materials under Award No. DE-SC0023124. Z.S. was supported by ERC-CZ program (project LL2101) from Ministry of Education Youth and Sports (MEYS) and used large infrastructure from project reg. No. CZ.02.1.01/0.0/0.0/15\_003/0000444 financed by the EFRR. K.W. and T.T. acknowledge support from the JSPS KAKENHI (Grant Numbers 21H05233 and 23H02052) and World Premier International Research Center Initiative (WPI), MEXT, Japan. M.J. acknowledges support from IITP grant funded by the Korean government (MSIT) (2021-0-01511). This work was performed, in part, at the Integrated Sciences Cleanroom and Nanofabrication Facility at Boston Col- lege.